

The investigation on Magnetic Activity of HD 134319 based on TESS Photometry and Ground-based Spectroscopy

Fukun Xu^{1,2*}, Shenghong Gu^{1,2,3*} and Panagiotis Ioannidis⁴

¹Yunnan Observatories, Chinese Academy of Sciences, Kunming 650216, China

²Key Laboratory for the Structure and Evolution of Celestial Objects, Chinese Academy of Sciences, Kunming 650216, China

³School of Astronomy and Space Science, University of Chinese Academy of Sciences, Beijing 101408, China

⁴Hamburger Sternwarte, Universität Hamburg, Gojenbergsweg 112, D-21029 Hamburg, Germany

Accepted xxx. Received xxx; in original form xxx

ABSTRACT

We present analysis of the starspot properties and chromospheric activity on HD 134319 using high precision photometry by TESS in sectors 14–16 (T1), 21–23 (T2) and high-resolution spectroscopy by OHP/ELODIE and Keck/HIRES during years 1995–2013. We applied a two-spot model with GLS determined period $P = 4.436391 \pm 0.00137$ day to model chunks sliding over TESS light curve, and measured relative equivalent widths of Ca II H and K, H β and H α emissions by subtracting overall spectrum from individual spectrum. It was found that a two-spot configuration, i.e. a primary, slowly evolving and long-lasting spot (P) plus a secondary and rapidly evolving spot S, was capable of explaining the data, although the actual starspot distribution is unable to derived from collected data. Despite the spot radius-latitude degeneracy revealed in the best-fit solutions, a sudden alternation between P and S radii followed by gradual decrease of S in T1 and the decrease of both P and S from T1 to T2 were significant, corresponding to the evolution of magnetic activity. Besides, S revealed rotation and oscillatory longitude migration synchronized to P in T1, but held much larger migration than P in T2. This might indicate the evolution of internal magnetic configuration. Chromospheric activity indicators were found to tightly correlated with each other and revealed rotational modulation as well as a long-term decrease of emissions, implying the existence and evolution of magnetic activity on HD 134319.

Key words: starspots – stars: chromospheres – stars: magnetic fields – stars: rotation

1 INTRODUCTION

Stellar magnetic activity arising from the enhancement of magnetic flux generated at the tachocline, penetrated the outer convection zone and then exceeded the surface of late-type stars manifests itself in abundant phenomena, such as starspots, plagues and flares, causing series of distortions detectable in both photometric and spectroscopic observations. Periodic or quasi-periodic variations in photometric measurements of cool stars are widely attributed to the rotational modulation of starspots. This makes starspot a good tracer of stellar rotation and detector of differential rotation which plays a critical role in generating and maintaining the solar-like magnetic activity through an $\alpha\Omega$ dynamo (Işık et al. 2011). Meanwhile, emissions of chromospheric activity indicators such as the Ca II H & K resonance and Balmer lines are generally used as diagnoses of magnetic activity in stellar outer layers and also show modulation under stellar rotation (Vida et al. 2015).

In analogy to the case of the Sun, the magnetic activity on active stars is believed to reveal both spatially inhomogeneous distribution and temporally evolution. The former creates inhomogeneous configuration of the magnetic field accompanying by the emergence of photospheric starspot and chromospheric excitation (Hempelmann et al. 2016; Balona et al. 2019), while the latter exhibits as evolution of starspot in terms of emerging, migrating, decreasing and vanishing during its life as well as the variation of chromospheric proxies in multiple timescales (Mittag et al. 2019). By long-term monitoring on photometric and spectroscopic variations, one can derive the starspot distribution, evolution and its connection with the chromospheric activity, which were reported on several targets and believed to be widely existed on late-type stars (e.g. Vida et al. 2015; Morris et al. 2018; Xu et al. 2021). However such a study is usually non-trivial due to the limit in acquiring high precision data of target in distance.

In recent years, space-borne telescopes such as MOST (Walker et al. 2003), CoRoT (Auvèrgne et al. 2009), Kepler (Koch et al. 2010) and most recent Transiting Exoplanet Survey Satellite (TESS, Ricker et al. 2015) produced bulk of long-term photometric data. Since its initiation, TESS was

* Email: xufukun@ynao.ac.cn(FX); shenghonggu@ynao.ac.cn(SG)

designed to cover $> 80\%$ of the whole sky and deliver light curves (LCs) spanning from 27 days to years for millions of stars, providing us the opportunity to analyse the starspot configuration and its evolution on stellar photosphere with high-precision (Reinhold et al. 2013; Namekata et al. 2020).

The star HD 134319 (TIC 202426247, GJ 577, Gl 577, HIP 73869, with magnitude $V = 8.41$ mag, $G = 8.23$, and color $B - V = +0.677$), is a young (~ 0.625 Gyr, Montes et al. 2001; McCarthy et al. 2001; Decin et al. 2003) active G5 main-sequence star of BY Dra type (Soderblom 1985) which can be taken as a young solar analogue with a shorter period of about 4.448 day (Messina et al. 1998). Locating in the north semi-sphere, was observed in six sectors by TESS (14–16 and 21–23) spanning over 300 days, revealing significant active regions surviving over 90 days as well as evidences of evolution in both short and long timescales. HD 134319's stellar parameters were greatly summarized in SIMBAD¹ and ExoFOP² and some of them are listed in table 1. The age of HD 134319 was firstly deduced as 0.625 Gyr by classifying it as a member of the Hyades supercluster in terms of space motion by Montes et al. (2001) and McCarthy et al. (2001), while other values from high-resolution echelle spectra were determined by Valenti & Fischer (2005) (6.3 Gyr), Takeda et al. (2007) (2.36 Gyr) and lastly Isaacson & Fischer (2010) (0.06 Gyr). Besides, a young nearby companion binary system, with GAIA magnitude of $G = 14.25$, and separation of $5.39 \pm 0.02''$ from HD 134319, was detected by infrared imaging (McCarthy et al. 2001; Mugrauer et al. 2004) and adaptive optics (Lowrance et al. 2003) (see section 2.2). The radial velocity (RV) of HD 134319 was firstly determined as $V_R = -3.8$ km/s by Wilson & Joy (1950), and most recently derived from OHP/ELODIE data with value $V_R = -6.362 \pm 0.011$ km/s, which was included in catalogue of RV standard stars by GAIA (Soubiran et al. 2018). Its long-term stability from 2002 to 2013 was reported by Butler et al. (2017) in their RV exoplanet survey using precision RV measurements by Keck/HIRES.

The chromospheric activity of HD 134319 was recognized by several studies (Soderblom 1985; Duncan et al. 1991; Wright et al. 2004; López-Santiago et al. 2010; Butler et al. 2017; Morris et al. 2019), by measuring its Ca II H & K emissions in terms of S-index and/or its corresponding derivative $\lg R'_{HK}$, giving typical median values of $S \sim 0.42$ and/or $\lg R'_{HK} \sim -4.12$, which indicates HD 134319 to be likely an ultra-active star (Boro Saikia et al. 2018). While the spot coverage on HD 134319 was reported to be very small through estimation of TiO molecular band absorption by Morris et al. (2019) in their investigation of the connection between activity level and spot coverage, they noted HD 134319 as an outlier with high activity but small spot coverage.

The starspots on HD 134319 from photometric analysis were firstly proposed by Messina & Guinan (1998) who clarified the increase of peak-to-peak amplitude of LC towards decreasing wavelengths to the presence of spots. Soon Messina et al. (1998) used rotational modulation to predict long-lasting active longitudes and spot covering fraction of at least $f_s \geq 0.16$ for this BY Dra type variable by employing

Table 1. Stellar parameters of HD 134319 in literatures.

Parameter	Value
RA, DEC	15h05m49.90423, +64°02'49.9415" ¹
V mag	$V=8.41$ ¹
Radius (R_{\odot})	0.94^a , 0.92984998^b , 0.92985^2
Mass (M_{\odot})	1.01^2
T_{eff} (K)	5668.04^2 , 5635.87^a , 5662^c , 5636^d
Metallicity [Fe/H]	$0.03^{1,2}$
$\log g$	4.50556^2
$v \sin i$ (km/s)	10.6^c , 17.89^e , 11.39 ± 0.06^f , 10.9^d

^a(Gaia Collaboration 2018), ^b(Stassun et al. 2018), ^c(Valenti & Fischer 2005), ^d(Morris et al. 2019), ^e(White et al. 2007), ^f(López-Santiago et al. 2010).

light curve inversion to multi-band (u, v, b and y, Strömgren 1966) photometric data spanning from 1991 to 1995. Later Messina et al. (2001) investigated the rotation-activity connection from photometry, including HD 134319.

In a word, the youth and high level of chromospheric and photospheric magnetic activity on HD 134319 make it a good proxy for the young Sun not far after its arrival at the zero age main sequence. In this paper we present a detailed analysis of starspot configuration, its evolution and chromospheric activity on HD 134319, using high-precision LC newly observed by TESS and collected spectroscopic data. In section 2, we introduce both the photometric and spectroscopic observations. We describe our approach for sliding spot modelling and the method for measuring relative equivalent widths from spectroscopic data in section 3. We then give the results and respective discussions in section 4, and finally the conclusions are summarized in section 5.

2 DATA AND REDUCTION

2.1 Spectroscopy

The spectroscopic data for HD 134319 collected online consist of two parts. One is the observations publicly accessible and available for download from Keck Observatory Archive³, which were carried out during years 1999 - 2013 by the HIRES spectrometer on the Keck I-10m telescope (Keck/HIRES, Vogt et al. 1994). The spectral resolution is about $R = 67000$. The other is the data from ELODIE Archive⁴ which was observed by ELODIE spectrograph on the 1.93m telescope of Observatoire de Haute-Provence (OHP/ELODIE, Baranne et al. 1996; Moutaka et al. 2004). The spectral resolution is 42000. Totally 26 spectra of OHP/ELODIE observed during years 1995 - 1997 and 22 spectra of Keck/HIRES observed during years 1999 - 2013 were collected.

Reduction of the raw data from Keck/HIRES was carried out using standard tasks in the IRAF package⁵, which basically included flat-field division, scattered light correction and wavelength calibration. The bias and dark corrections

³ <https://koa.ipac.caltech.edu/>

⁴ <http://atlas.obs-hp.fr/elodie/>

⁵ IRAF is distributed by the National Optical Astronomy Observatories, which is operated by the Association of Universities for Research in Astronomy (AURA), Inc, under cooperative agreement with the National Science Foundation.

¹ <http://cdsweb.u-strasbg.fr/>

² <https://exofop.ipac.caltech.edu/tess/target.php?id=202426247>

were omitted due to their absence in some spectra, and that flat corrections were done using flats with wide orders (there existed another type of flats with narrow order in a fraction of observations).

OHP/ELODIE provides two types of products: the combined one dimensional spectrum (*s1D*) which was uniquely resampled in wavelength and given in instrumental relative flux covering 4000 to 6800 Å, and the two dimensional image (*s2D*) which contains the extracted and deblazed spectrum in 67 orders.

According to wavelength coverage, we chose the spectral portions around Ca II H & K, H β and H α lines. For Keck/HIERS, H α is available since 18 August 2004. For OHP/ELODIE *s2D* data, H β portion was selected from order 32 (H β in order 31 was omitted due to bad pixels H α portion was selected from order 64, and Ca II H & K (in orders 3 and 2, respectively) were omitted due to low signal to noise ratio (SNR).

2.2 GJ 577 B/C

A young nearby proper motion companion of HD 134319, with separation of $5.39 \pm 0.02''$ to the west and GAIA magnitude of $G \sim 14.25$, was detected by infrared imaging (McCarthy et al. 2001; Mugrauer et al. 2004) and adaptive optics (Lowrance et al. 2003). Mugrauer et al. (2004) determined its spectral type as *M4.5*, mass as $0.16 - 0.20 M_{\odot}$, age as > 100 Myr and found its strong H α emission and deep TiO and VO molecular absorption bands. Lowrance et al. (2003) further recognized it as a binary system (GJ 577 B/C) with separation $0.082''$, both of which lie on the stellar/substellar boundary with spectral type between *M5V* and *M6V*. This scenario of binary system was also noted by Burgasser et al. (2005) and Martin et al. (2017) and confirmed by proper motion anomaly (Kervella et al. 2019).

The separation of $5.39''$ is apparently far enough in spectroscopy on Keck/HIRES⁶ and OHP/ELODIE⁷ and thus unlikely to contaminate the primary's spectra. However the companion is near enough in TESS photometry (spatial resolution of $21''/\text{px}$ ⁸) to be crowded in the same pixel as the primary. For simplicity we assume that it will not put detectable distortion, but at most a small offset about 0.40%, on resultant TESS LC because it is much fainter ($G = 14.25$) than the primary ($G = 8.23$) as measured by GAIA (Gaia Collaboration et al. 2018).

2.3 TESS Light Curve

The TESS mission (Ricker et al. 2015) was designed to observe an extremely wide sky area in sectors measuring $24 \times 96^\circ$, utilizing four wide-field cameras aligned in a mosaic, extending from near the ecliptic equator to beyond the ecliptic pole. The initial two-year observation strategy of TESS includes 26 sectors, each of which is observed in two highly elliptical 13.7 day orbits around the Earth, spanning about 27 days. TESS provides simple aperture photometry

(SAP) and pre-search data conditioning (PDC) processed LC generated from two-minute cadence data, processed by NASA's TESS Science Processing Operations Center (SPOC) pipeline (Jenkins et al. 2016) which is a successor of Kepler's pipeline⁹, as well as the calibrated target pixel file (TPF, which contains the pixel level photometric time series). All of them are publicly accessible and available for download from Mikulski Archive for Space Telescopes (MAST) at STSci data base¹⁰ to ensure simultaneous usage of final products and check of the data quality in pixel level.

Considering that the PDC process was primarily designed for planet hunting but not for the study of stellar variabilities which usually show non-unique and much broader periodic durations and variations than planetary transits, and could be ignored or misinterpreted by the pipelines, it is generally recommended to check the systematic correction by PDC and redo it when necessary (Still & Barclay 2012; Vinićius et al. 2017). We used calibrated TPFs to check whether the pipeline chosen apertures, which are different between sectors, can overcome the possible contamination from the crowded neighbours and temporal variation of photons distribution, i.e., whether the PDC processed LC is suitable for stellar activity investigation.

The determination of optimal aperture in wide field-of-view photometry like TESS (Ricker et al. 2015) is non-trivial due to the crowdedness of objects versus wide spread image of stars on CCD. Crowdedness contributes to extra flux on target and should be avoided by employing smaller aperture, which, however, causes wastage of the target flux and leads to lower SNR. Estimations of *flux fraction* and *crowding matrix* were done by PDC to recover the real brightness of target in Kepler and later TESS (Batalha et al. 2010). However the automatically predetermined aperture and its correction in pipeline might be unsuitable for individual case, as widely revealed (for example, the large jumps between adjacent sectors) on many targets (e.g. Özavcı et al. 2018; Xu et al. 2021), and should be checked with caution, especially in investigation of stellar variation.

HD 134319 was observed by TESS in sectors 14–16 and 21–23 during its second year's routine. Besides GJ 577 B/C, there are other three neighbours (1620024559829845504, 1620023597757174144 and 1620024692973605760) matched with *Gaia* DR2 (Gaia Collaboration et al. 2016, 2018) around HD 134319 recorded on the CCD image of TPFs. The last two are far enough from HD 134319 and properly excluded by PDC. The first one ($G_{\text{mag}} = 13.9574$, fainter than HD 134319 by about two orders of magnitude) was excluded outside the PDC apertures in sectors 14–16, but not in sectors 21–23 due to the variation of flux spread. Considering that no recognizable difference in profile of whole LC between with and without this neighbour was found, we concluded that it does not contribute detectable contamination on HD 134319's LC.

Moreover, we assessed the validity of PDC determined apertures by comparing the LC profiles derived from different apertures. One can manually define a smaller TPF masks, i.e. photometric apertures, by setting a larger value of parameter *threshold*, which defines the threshold in choosing the pixels

⁶ <https://www2.keck.hawaii.edu/inst/hires/slitres.html>

⁷ <http://www.obs-hp.fr/www/guide/elodie/elodie.html>

⁸ <https://heasarc.gsfc.nasa.gov/docs/tess/observing-technical.html>

⁹ <https://heasarc.gsfc.nasa.gov/docs/tess/>

¹⁰ <https://mast.stsci.edu/>

to be integrated in LIGHTCURVE, and vice versa. We found that the profile of integrated LC was stable with masks both slightly smaller and larger than the PDC, indicating that the spread function of HD 134319 was stable over time and the apertures determined by PDC were suitable for our study.

Consequently, we used the PDC corrected LC, i.e. *PDC-SAP* long cadence data, in our analysis. There was no empirical evidence of improper correction by PDC for all sectors except two parts with improper offsets. One is the first half of sector 22 (1899 – 1927 after BTJD – 2457000) and was subtracted by an offset of 400 ADU, the other is sector 23 and was added by an offset of 1000 ADU. This kind of offset, to remove the discontinuities between the improper segment and its surrounding LCs, was estimated qualitatively due to the too short time length of segment to adopt a semi-quantitative method (e.g. [Özavcı et al. 2018](#)). The possible under- or over-estimation of the offset attributes to a common deviation of LC, which results in either spot size variation or additional polar spot but has not much to do with the spot evolution. At last the LC was normalized to unity by dividing its median over the whole time span (figure 1).

3 MODEL AND ANALYSIS

3.1 Modelling the light curve

Periodic or quasi-periodic variation in photometric LC is generally attributed to the starspot rotating into and out of view from Earth ([Valio et al. 2017](#)). As a manifestation of internal magnetic flux on the stellar surface, starspot generates notable distortion on LC which makes it as good indicator of the internal magnetic structure and tracer in measuring the surface rotation. However, reconstructing two-dimensional distribution of the starspots from one-dimensional disk-integrated photometric time series is always not easy due to the weak constraints from the observation itself ([Lanza et al. 2016](#)) as well as the large parameter space and high degeneracy between parameters of spot model. One should to reduce the number of parameters as small as possible in spot modelling and treat the results with caution.

3.1.1 Rotational period of HD 134319

In literatures (table 2), the rotation period of HD 134319 was reported as 4.448 day by [Messina & Guinan \(1998\)](#) and 4.43 day by [Wright et al. \(2011\)](#) from photometric observations, and estimated as 5.0 day by [Wright et al. \(2004\)](#) and 3 day by [Isaacson & Fischer \(2010\)](#) from statistical determination of chromospheric activity fluctuations. With the favour of long-term precise photometry by TESS, we can obtain an accurate measurement of the period revealed by the rotational modulation. We used the generalized Lomb-Scargle periodogram (GLS, [Zechmeister & Kürster 2009](#)) to measure the period of time series in sectors 14–16 and 21–22 of TESS (sector 23 was temporarily excluded due to its empirically questionable LC) as $P = 4.436391 \pm 0.00137$ day, which is slightly larger than the one of [Wright et al. \(2011\)](#) and smaller than the one of [Messina et al. \(1998\)](#).

In figure 2 we show the phase-folded LC of HD 134319 using this rotation period. Two dips in brightness per rotation with different depths are visible throughout the observation

Table 2. Rotational periods of HD 134319 measured by different authors.

Reference	Period (days)	Memo
Messina et al. (1998) ^a	4.448 ± 0.005	^b
Wright et al. (2004)	5.0	cf. R'_{HK}
Isaacson & Fischer (2010)	3	cf. R'_{HK}
Wright et al. (2011)	4.43	^c
This work	4.436391 ± 0.00137	^d

^aAlso in [Messina & Guinan \(1998\)](#); [Messina et al. \(2001\)](#), ^bphotometric Scargle-Press period ([Scargle 1982](#)), ^cphotometric period by FEPS ([Meyer et al. 2006](#)), this value was cited by [Butler et al. \(2017\)](#); [Mittag, M. et al. \(2018\)](#); [Morris et al. \(2019\)](#), ^dphotometric period by GLS ([Zechmeister & Kürster 2009](#)).

age. The primary dip ("P") is visible over the whole observation season, starting from Phase ~ 0.7 at onset and shifting gradually to Phase ~ 0.5 in the end. The secondary dip ("S"), emerging at Phase ~ 0.3 at onset, is recognizable before time 1763.5, then becomes ambiguous after that due to its small amplitude. On the other hand, notable decrease in brightness loss of both "P" and "S" can be found with increasing time, revealing notable evolution of spot configuration.

3.1.2 GEMC_LCM

As an analytical model towards photometric observation, light curve modelling (LCM, [Budding 1977](#); [Dorren 1987](#)) simulates the LC with assumption that the drop in light intensity is caused by a small number of circular spots occupying on the stellar photosphere and thus is capable of reducing the parameter space to some extent. LCM consists of parameters relative to the star (the unspotted intensity U , the linear limb-darkening effect u and the inclination i) and individual circular spot (the spot-to-photosphere intensity ratio κ_w , the spot latitude β , longitude λ , radius γ and its rotational modulation period P). Practically stellar parameters i , U and u are constants and parameter κ_w can be approximately constants and common to all spots. Taking into account the rotation, the periodical variation of longitude can be better defined as a function of of time t by the rotational period P and initial longitude $\lambda(0)$ as $\lambda(t) = 2\pi t/P - \lambda(0)$ for convenience ([Xu et al. 2021](#)).

An efficient program, called "GEMC_LCM" ([Xu et al. 2021](#)), which was designed to inherit both the superior global optimization power of genetic algorithm and the high efficiency on parameter space exploration of Markov Chain Monte Carlo algorithm, was employed for spot modelling using LCM of [Budding \(1977\)](#). GEMC_LCM is able to run parallelly on mulit-core CPU with the favour of OPENMP.

3.1.3 Parameter degeneracies

Besides the large parameter space, the parameter degeneracies in spot modelling are another kind of problem in photometry modeling, which block the algorithm converging to the true solution. Practically it is difficult to overcome this problem in spot modelling in the absence of independent constraints. However it is reasonable to divide such degeneracies into two types according to their sources, i.e., they are inherent or produced. The former comes from the model in-

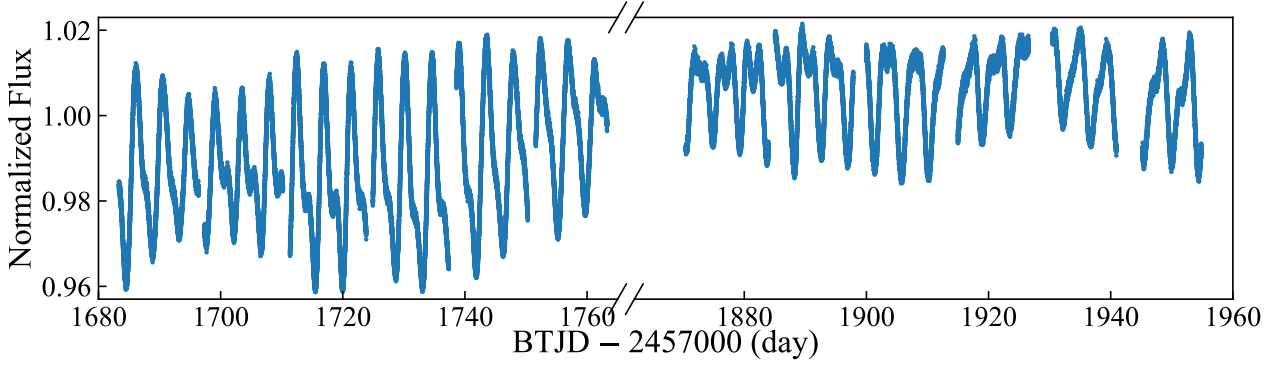


Figure 1. Resultant light curve.

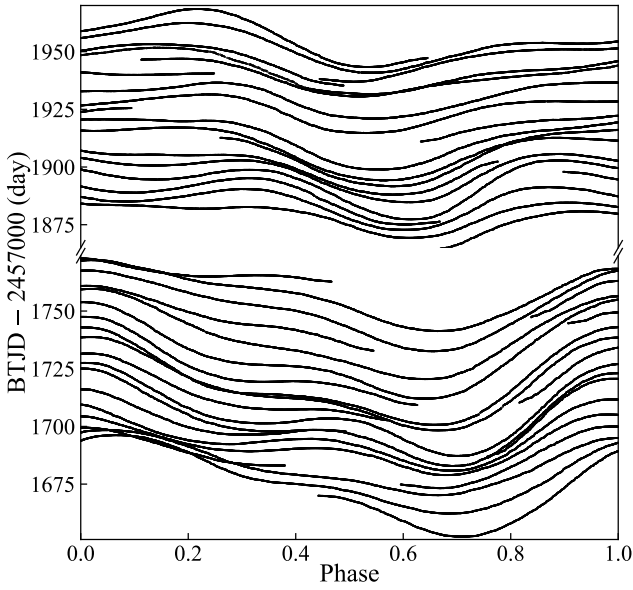


Figure 2. Phase-folded, median smoothed LCs for HD 134319 with GLS estimated rotation period $P = 4.436391$ day, showing a larger, primary "P" plus a smaller, secondary "S" condensed regions under starspot modulations and their notable evolution over time. The vertical position for each curve corresponds to the start time of chunk. Each time window is scaled to larger amplitude for easier view by subtracting 1 then multiplying it by 800, i.e. $f' = 800(f - 1)$. The long-time gap from 1763.5 to 1869.5 is marked by breaks in vertical axes.

self, while the latter comes from measurement related effects which can be suppressed by high precision photometry.

An inherent degeneracy between stellar inclination and spot latitudes was identified from numerical simulation by Walkowicz et al. (2013), who also showed the possibility of failure in detecting the differential rotation when LC is dominated by one large active region. Actually, when it comes to the case of LCM with single spot, one can easily find that this degeneracy can be expressed analytically as

$$I_c(i, \beta) = I_c(90^\circ - |\beta|, \text{Sign}[\beta](90^\circ - i)) \quad (1)$$

Where I_c is the simulated LC, $\text{Sign}[\beta]$ means the sign of β , and specially $\text{Sign}[0] = \pm 1$. In other words, the spot at

latitude β with inclination i creates definitely the same LC as spot at latitude $\text{Sign}[\beta](90^\circ - i)$ with inclination $90^\circ - |\beta|$.

A produced degeneracy between spot latitude and radius due to the low constraint of photometry versus noise and contamination was noted as an "ill-posed" issue (Lanza et al. 2016). For example, a larger spot at higher latitude distorts the LC with similar amplitude as a smaller spot at lower latitude by means of projection to light of sight. However, it is possible to minimize such a defect to some extent with the mercy of high precision photometry as they lead to subtle but different profiles in principle (Walkowicz et al. 2013). Besides, the contamination coming from the residual systematic errors in long-term observations such as Kepler and TESS can be mixed with stellar variations in multiple timescales. Thus it is usually recommended to do the systematic error corrections, circumstances alter cases, in stellar variation investigations (Still & Barclay 2012; Vinicius et al. 2017). We have checked the LC as described in section 2.3.

To derive the properties of spot configuration independent on parameter degeneracies, it is feasible to employ some assumptions a priori. A predefined stellar inclination is capable of breaking its degeneracy with spot latitude. The stellar inclination can be calculated from measured $v \sin i$, stellar radius R and rotation period P by

$$i = \arcsin(v \sin i * P / 2\pi R) \quad (2)$$

With the measured period $P = 4.436391$ day as derived in section 3.1.1, the stellar radius in table 1 implies a maximal $v \sin i \sim 10.7$ km/s. Considering that the projected rotational velocity $v \sin i$ was estimated in the range between 10.6 km/s and 17.89 km/s (table 1), HD 134319 is preferred to have a high inclination. As a comparison, we adopted fixed inclination of $i = 75^\circ$ and $i = 90^\circ$ in modelling.

3.1.4 Surface differential rotation

The differential rotation was thought to play a critical role in generating and maintaining the stellar magnetic field. The surface differential rotation (SDR) on the Sun was observed in relative motion of sunspots and can be expressed by a quadratic law

$$P(\beta) = P_{\text{eq}} / (1 - \alpha \sin^2 \beta) \quad (3)$$

Where $P(\beta)$ is the stellar rotation period at latitude β , P_{eq} is the reference period at equator, and α is relative rate repre-

senting the strength of SDR, which was measured as $\alpha = 0.2$ on the Sun. A similar law of SDR is generally assumed on stars other than the Sun by analogy (Henry et al. 1995). By this definition a zero α means a rigid rotation, a positive α represents a Solar-like SDR while a negative α represents an anti-Solar SDR.

3.1.5 Spot modelling

The whole LC was split into chunks with 5 days duration each, slightly longer than one rotation period, and advanced by 1 day forward, providing a total of 129 such chunks for spot modelling. In such a short timescale, the spot positions are not expected to evolve, while their radii are allowed to change linearly indicated by the apparent variation of LC within adjoint rotations.

The modelling was done under hypothesis of a stellar sphere with uniform surface brightness occupied by circular dark spots with uniform temperature. The pre-determined parameters were chosen as follows. The limb darkening effect was assumed to be a linear law with coefficient $u = 0.5119$ from the table of Claret (2018) for a star with $T_{\text{eff}} \sim 5600 \text{ K}$ and $\log g \sim 4.5$. The uniform spot-to-photosphere intensity ratio was fixed to $\kappa_w = 0.22$ empirically derived from statistics (figure 7 of Berdyugina (2005)). The stellar surface brightness was also fixed as the maximal value of LC, $U \sim 1.02$, which is artificial to some extent because the target is always occupied by spots. At last, by comparison, we employed two values of stellar inclination $i = 75^\circ$ and $i = 90^\circ$.

The spot configuration in each chunk was derived under a two-spot model. The number of spots was determined by two reasons. One is that there are two minima in almost all chunks, probably inferring a distribution of two concentrated active regions on the surface. The other comes from our tests in checking the global optimizing capability of models with two and three spots. It was found that three (or more) spot model provided slightly better fitting as expected, while resulted more likely in families of solutions with equally good fits which reduces its reliability, comparing with two-spot model. Therefore a two-spot model was sufficient to obtain acceptable fits. Note that, strictly speaking, the real number of spots (or active regions) might or might not equal to the number of minima in LC (Jeffers & Keller 2009; Basri & Shah 2020), but we would rather to fit the LC with a simple spot-model for efficiency and convergence of optimization, and if the spot distributions on the star can be described by such a two-spot model it would be the result.

The determination of rotational modulation period corresponding to spot is non-trivial. Usually it can be determined with high precision due to the strong constraint of long-term photometric time series on longitude, despite exceptions, e.g. when one spot dominates the LC (Walkowicz et al. 2013). However, such a constraint becomes weak in our case when we do spot modelling for single chunk, i.e. in pretty short timescale. Instead we adopted fixed period in modelling after several numerical experiments, and thus the derived longitude might vary due to two effects, i.e. the evolution of spot longitude, and the difference between the chosen and actual rotational modulation period of spot.

As a conclusion, we employed a two-spot model to inverse the longitudes, latitudes, linearly evolving radii of spots (i.e. eight free parameters in total) for each chunk, using fixed pe-

riod $P = 4.436391$ day. For the sake of higher probability of globally optimized solution, each chunk was fitted for many runs, and the results were then divided into groups corresponding to different spot configurations. Finally we elected the group with minimal combined residuals $\sum_j (\chi_j^2)$ summing over all chunks (j) as the final result.

3.2 Relative variations of chromospheric activity

Core emissions in strong optical spectral lines, such as the Ca II H & K and H α lines, are proven proxies for magnetic flux on the Sun (Eberhard & Schwarzschild 1913). Their strengths as well as variations were used for monitoring stellar activity levels and detecting long-term activity cycles similar to the solar 11 year's cycle. For example, the S-index, developed by the Mount Wilson Observatory HK Project (Duncan et al. 1991), is a measure of the emission in the Ca II H & K line cores in the lower to middle chromosphere due to magnetic heating, and was widely used in measuring the stellar rotation period as well as the long-term activity cycles (e.g. Hempelmann et al. 2016; Butler et al. 2017; Mittag, M. et al. 2018; Mittag et al. 2019).

3.2.1 Approach

According to the wavelength coverage of spectra, we adopted the Ca II H & K, H β and H α lines to measure chromospheric activity. The spectral subtraction technique (Barden 1985; Montes et al. 1995) has been widely used in measuring their emissions with the favour of comparison star or synthesized spectrum (e.g. Montes et al. 1995; Gu et al. 2002; Cao et al. 2019). However, noting the difficulty in finding the continuum around the Ca II H & K lines (Shkolnik et al. 2005) while the requirement of precise measurement on temporal variations of chromospheric activity indicators in our case, we alternatively employed a scheme based on Xu et al. (2021), which is capable of deriving relative variation of equivalent widths of chromospheric activity indicators in series of spectra with high precision.

The scheme consists of following steps. **1.** Delete outliers in each spectrum contaminated by cosmic rays, telluric lines, CCD bad pixels, etc. **2.** Normalize the spectrum with highest SNR to unity as reference spectrum F_R . **3.** Fit other individual spectra $F'(\lambda')$ by a product of $F_R(\lambda)$ and a polynomial $P(\mathbf{a}; \lambda - \lambda_0)$, i.e. $F'(\lambda) = P(\mathbf{a}; \lambda - \lambda_0)F_R(\lambda)$ where λ_0 is the reference wavelength, and then apply a shift $\Delta\lambda$ due to RV, i.e. $\lambda' = \lambda + \Delta\lambda$. Each individual spectrum is inversely transformed to unity F_U using derived parameters \mathbf{a} and $\Delta\lambda$. **4.** The overall spectrum F_M is obtained as the median over a subset of spectra with high SNR. Then the residual spectrum is $f = F_U - F_M$. **5.** Correspondingly the relative equivalent width is $\Delta W = W - W_M = -\int f d\lambda$. By fitting f with a Gaussian function, $g(\lambda) = A \exp[-(\lambda - \lambda_0)^2/(2\sigma^2)]$, we have $\Delta W = -\sqrt{2\pi}A\sigma$. Note that minus value means emission.

Figure 3 shows two example spectra observed by HIRES/Keck at 20060416 and 20110615 (table 4), when all of Ca II K, H, H β and H α emission lines exhibited almost the most significant negative and positive residuals, respectively. The relative variation was small compared to the overall spectra but can be extracted with reliability by above scheme.

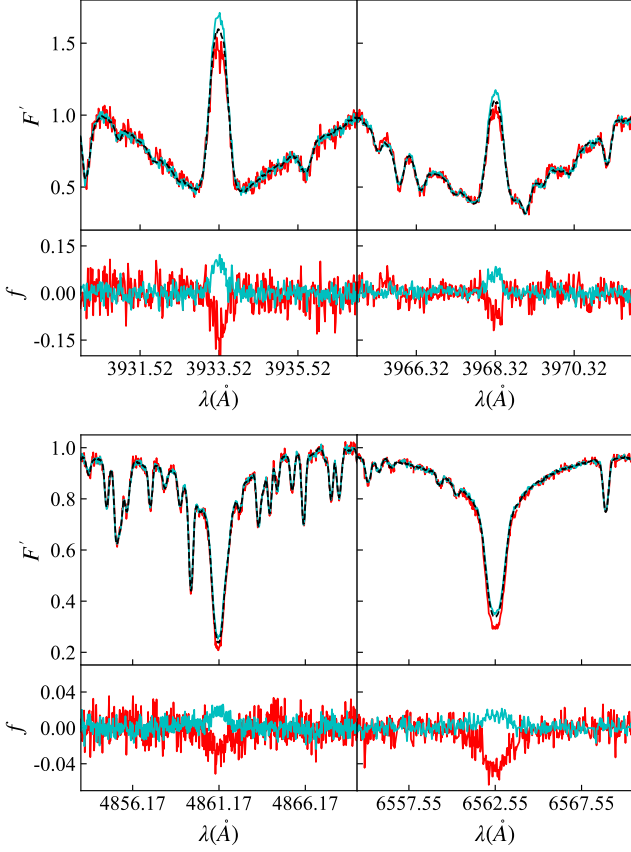


Figure 3. Examples of spectra observed at 20060416 (red line) and 20110615 (cyan line) reduced by our scheme. Each panel shows spectra F' derived by step 3 with the overall spectrum F_M overlaid by black dashed line, along with their respective residual spectra $f = F' - F_M$ derived by step 5.

By using subsets of Keck/HIRES spectra, [Wright et al. \(2004\)](#), [Isaacson & Fischer \(2010\)](#) and [Butler et al. \(2017\)](#) measured S-index of HD 134319 independently. Comparison between our measurements and their results is shown in figure 4, overlaid with respective linear fittings. Note that [Wright et al. \(2004\)](#) employed a scheme similar to us by using the highest SNR observation as a template in measuring the "sensitive differential S-values". Our result fits well with the ones of [Wright et al. \(2004\)](#) and [Isaacson & Fischer \(2010\)](#), indicating the reliability of our scheme in measuring the relative variation of chromospheric activity indicators.

3.2.2 Residual spectra

The parameters in above scheme were determined by numerical experiments and listed in table 3. In step 2, The reference spectrum was the one observed at Jan 27, 2008 (record 41 in table 4) by Keck/HIRES. In step 3, the background portions, whose length should be short enough for a good fitting by a low-order polynomial while long enough to include enough absorption lines to measure RV shift, were chosen as a compromise and the gap centred on respective emission core was temporally included for background fitting. In step 4, the subset used in calculating the overall spectrum F_M consists of

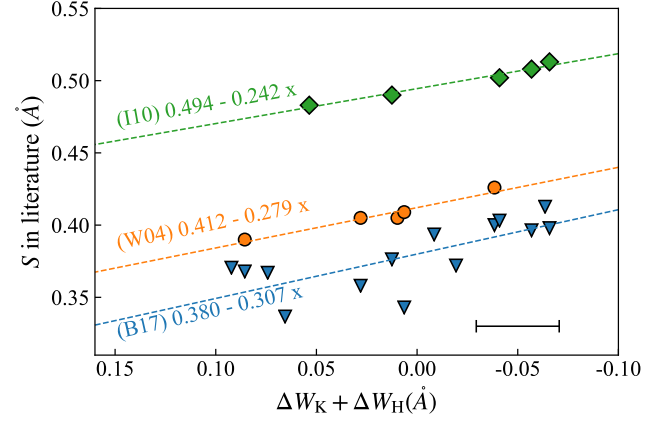


Figure 4. Comparisons between our measurements, $\Delta W_K + \Delta W_H$, and previous measurements of S-index from [Wright et al. \(2004\)](#) (W04), [Isaacson & Fischer \(2010\)](#) (I10) and [Butler et al. \(2017\)](#) (B17). Linear fittings to the three cases are overlaid. The horizontal error bar represents the typical uncertainty of our measurement.

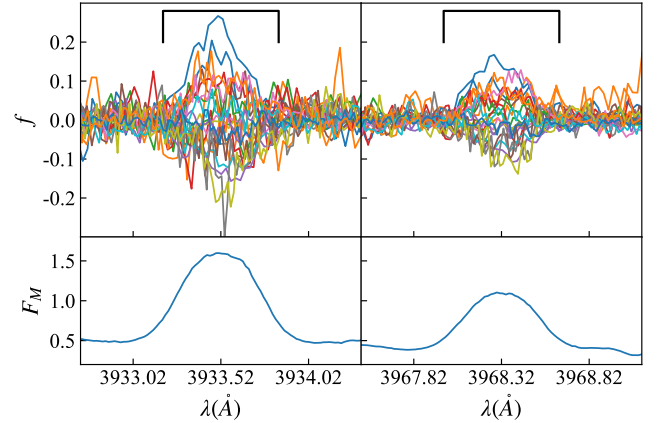


Figure 5. The residual spectra f (up panel) and the overall spectrum F_M (lower panel) ($f = F_U - F_M$) for Ca II K (left) and H (right). The typical width of Gaussian fit (corresponding to σ) in measuring relative equivalent width ΔW was over-plotted by black lines.

records 31–37, 39–41, 43, and 46–48 (table 4) with high SNRs and common to all indicators. In step 5, the width of Gaussian function, in accordance with σ , was estimated by plotting residual spectra f together and fixed as $\sigma = \text{FWHM}/2.35482$ for each index. The fitting interval within which Gaussian fitting was done was used to estimate the fitting errors.

Normalizations of Ca II H and K lines to unity through continuum division are usually questionable due to the difficulty in finding their continua, an alternative way was employed by fitting a straight line to the edges of spectral portion ([Shkolnik et al. 2005](#)), 7 \AA wide, centred on emission cores, respectively. Figure 5 shows the residual spectra f and their respective overall spectra F_M from Keck/HIRES. Emissions of resonance from F_M and variations of chromospheric activity from f are notable, indicating a high level of magnetic activity.

Table 3. Spectral fitting parameters.

Index	λ_0 (\AA)	Parameters in step 3 (Polynomial fit)		Parameters in step 5 (Gaussian fit)	
		Background portions ($-\lambda_0$)	Order	Fitting interval ($-\lambda_0$)	σ
Ca II K	3933.52	-7 - -0.75 and 0.75 - 7	2	-7 - 7	0.140
Ca II H	3968.32	-7 - -0.75 and 0.75 - 7	2	-7 - 7	0.140
H β	4861.17	-8 - -2 and 2 - 8	3	-8 - 8	0.425
H α	6562.55	-13 - -3 and 3 - 13	3	-13 - 13	0.828

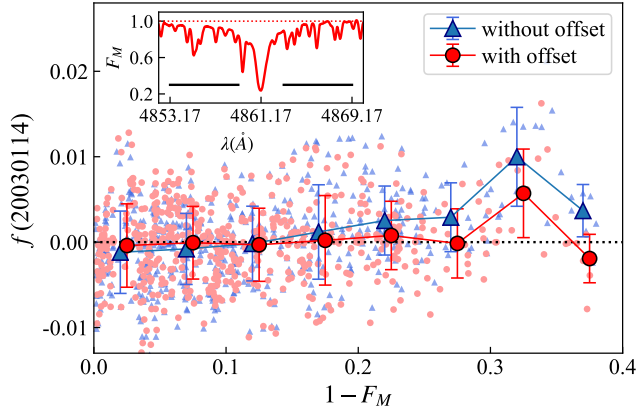


Figure 6. Comparison between residuals f with and without an offset o included in fitting $F'(\lambda')$ by $P(\mathbf{a}; \lambda - \lambda_0)F_R(\lambda) + o$ versus $1 - F_M$: the example of H β was observed by Keck/HIRES on Jan 14, 2003. The overlaid larger triangles and circles, horizontally misaligned from each other, were sliding average of respective smaller symbols, the error bar represents the standard deviation of corresponding interval. The overall spectrum is plotted in sub-window with background portions in table 3 overlaid with black lines.

H α and H β can be normalized to unity by general continuum division with reliability. Moreover, with the high quality of H β and H α lines by Keck/HIRES, we recognized an improper trend between fitted residuals and spectral absorption depth, i.e. the background portions in residual f , which might result from improper reduction, e.g. scattered light residuals, reflected by high SNR data. An offset is capable of fitting out such a trend mathematically, i.e. $F'(\lambda) \equiv o + P(\mathbf{a}; \lambda - \lambda_0)F_R(\lambda)$, and was included in processing H β and H α of Keck/HIRES spectra. Figure 6 shows example of H β with the most notable difference between with and without offset observed at Jan 14, 2003.

Figure 7 shows the residual spectra f and respective overall spectrum F_M of H β and H α lines, from which we can also see variable emissions with different amplitudes.

4 RESULTS AND DISCUSSION

It's unfeasible to decide the real number of starspots from disk integrated photometric observation. The number of dips in LC corresponds only to the lower limit of starspots number, because LC can always be fitted by model with as many starspots as one likes (Jeffers & Keller 2009; Basri & Shah 2020). One has to adopt a priori compromise to reduce the free parameter space and increase the possibility of conver-

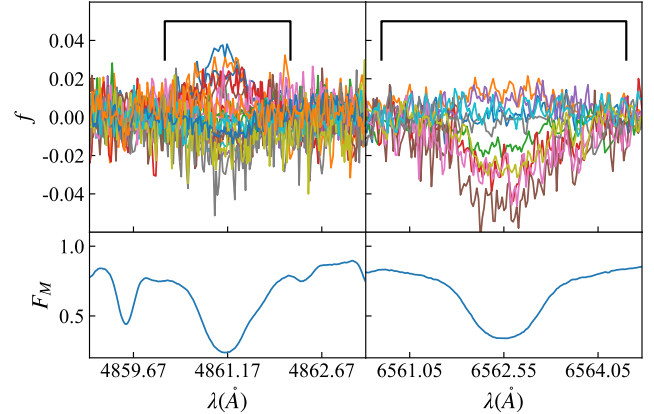


Figure 7. Same as figure 5, but for H β (left) and H α (right).

gence in optimization so as to obtain a reasonable solution in fitting. For example, LCM simulates the LC by an analytically model with a few circle spots, while light curve inversion (LCI) usually employs either the maximum entropy or Tikhonov criterion for a unique and stable solution (e.g. Lanza et al. (2006)). Thus, if the photosphere of HD134319 is covered by or equivalent to two dominant starspots (or active regions) versus surroundings with non-spot or stable distributed starspots contributing no rotational modulation, our result should reveal the distribution and relative evolution of starspots, or else it would rather be the description of hemispheric asymmetry.

4.1 Results comparison between different inclinations

Using the best-fit and manually checked solutions from many independent runs for each chunk, we were able to increase the probability of optimization to fall into global minima in limited iterations, and thus to trace the sizes and locations of starspots over the entire span of TESS data with reliability.

Practically, each chunk was modelled independently by 50 runs for inclination $i = 75^\circ$ and 40 runs for inclination $i = 90^\circ$. The solutions could be divided into a few groups characterized by special spot configuration. In most cases it was easy to elect the globally optimal solution by choosing minimal residual χ^2 , however outliers existed where local minima had equally good or even better fit than the predicted one. To overcome this problem we additionally assumed that spot configuration among adjacent chunks should be similar to each other as they shared about 80% data points.

By comparison, figure 8 displays the spot longitudes, lat-

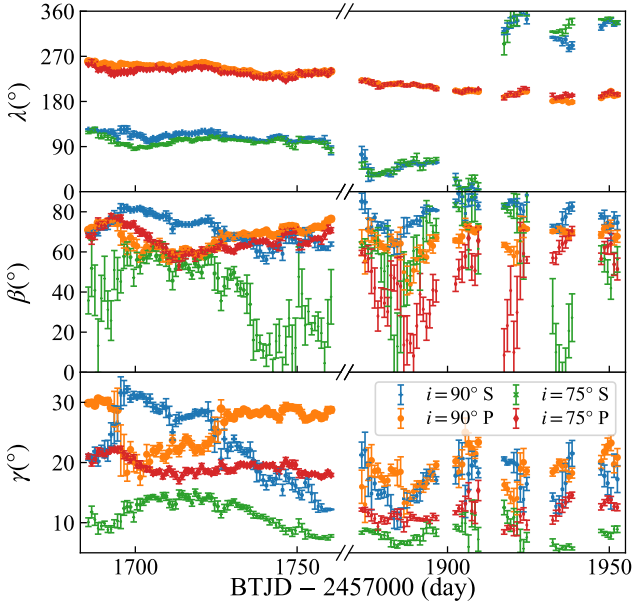


Figure 8. Temporal variations of spot longitudes (top), latitudes (middle) and radii (bottom) for inclination $i = 75^\circ$ (green crosses and red diamonds) and $i = 90^\circ$ (blue pluses and orange circles), respectively. The radius of each spot plotted, hereafter, takes its value at mid-epoch of respective chunk under the assumption of linearly evolving size. "P" represents the larger spot (primary) and "S" represents the smaller spot (secondary) in each case. The sizes of symbols are proportional to the spot radii.

itudes and radii corresponding with $i = 75^\circ$ and $i = 90^\circ$ respectively. Under assumption of linear evolution, we took the value of spot radius at mid-epoch of each chunk in plot and discussion hereafter.

The spot longitudes were derived with high stability for both cases as expected due to both the strong constraint of photometry on rotational phase and the orthogonality between stellar inclination and longitudes. Two active longitudes can be easily recognized i.e. the primary one (named "P") centring around longitude $\lambda \sim 220^\circ$ and the secondary one (named "S") varying around longitude $\lambda \sim 130 - 50^\circ$.

Two features can be found from the distribution of spot latitudes. First, the case of inclination $i = 75^\circ$ generally shows spots at lower latitudes than $i = 90^\circ$, which implies a mathematical deviation of configuration corresponding to input inclination, i.e., an evidence of parameter degeneracy. Second, the result shows similar relative variations of spot latitudes between input inclinations, which indicates a possible constraint of high accuracy by TESS photometry on spot latitudes versus noise, to some extent.

A degeneracy between spot radius and latitude is recognizable in both cases. Figure 9 shows the distribution of spot radius versus its latitude for "P" and "S" in different time ranges for inclination $i = 90^\circ$, and their comparison to simulations for a supposed spot at latitude $\beta = 70^\circ$ initially with series radii $\gamma = 13, 20, 23$ and 28° through setting the spot's latitude ranging from 40 to 85° . The highly coincidence between results and simulations within time range 1869–1995 indicates probable existence of degeneracy, while the apparent deviation within time range 1683–1764 from such a co-

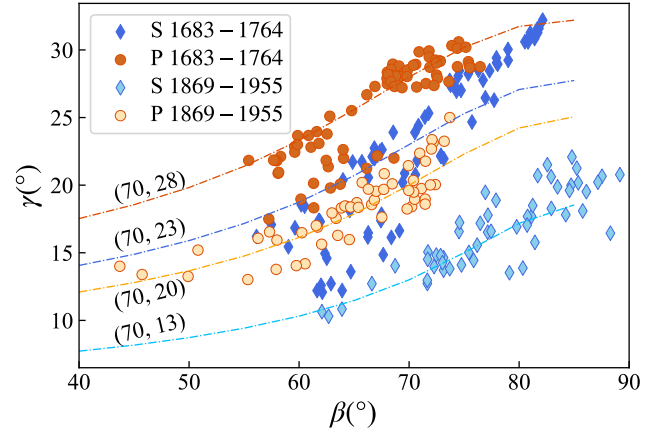


Figure 9. Spot radius–latitude ($\gamma - \beta$) correlation from best-fit solutions, different symbols represent spots "P" and "S" at different time ranges. The simulations for an artificial spot at latitude $\beta = 70^\circ$ initially with series radii $\gamma = 13, 20, 23$ and 28° through varying its latitude value from $\beta = 40^\circ$ to 85° are overlaid with dash-dot lines.

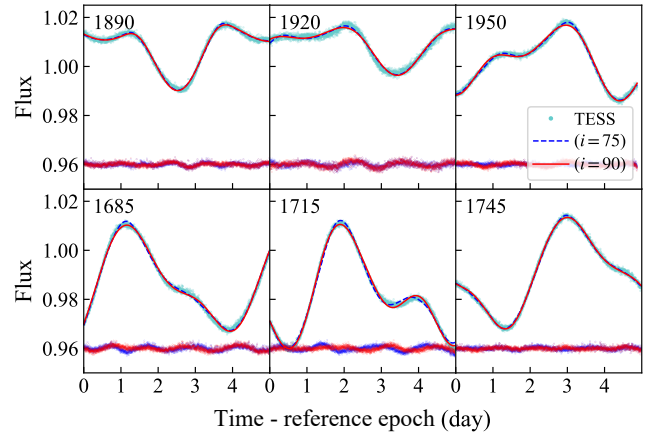


Figure 10. Illustration of modeling on inclinations $i = 75^\circ$ (blue dashed line) and $i = 90^\circ$ (red line) for TESS LC (cyan dots), one chunk for each sector, with epoch of each chunk indicated. The horizontal axis of each panel was modified to $0 - 5$ by subtracting its epoch. Residuals are over-plotted at value of 0.96.

incidence means reliable variation of either spot radius or latitude.

Figure 10 shows one fitting example in each sector for cases of inclination $i = 75^\circ$ and $i = 90^\circ$. Both cases reveal that good fits have typical residuals around $0.0001 - 0.0002$, implying that the spot configuration on HD 134319 can be reasonably described by two condensed active regions. As a whole, fitting of $i = 75^\circ$ resulted in slightly larger χ^2 than $i = 90^\circ$ in most chunks, which indicates an extremely high inclination of HD 134319, coinciding with the prediction from spectroscopy. Hereafter spot modelling result with inclination $i = 90^\circ$ is employed in discussion.

4.2 Starspot Evolution and Differential Rotation

4.2.1 Configuration of two active regions

In figure 11 we reproduce the continuous phase versus time evolution map of flux, with spot longitudes from the best-fit solution and their linear fittings overlaid. Two active regions characterized by their amplitudes of dip in brightness, i.e. the primary "P" located at phase about 0.71 and the secondary "S" located at phase of about 0.34, separating by 140° in longitude, are revealed to be located at high latitudes varying between 50 and 80 degrees (figure 8). The solutions also indicate the difference between spot sizes, and the smaller one evolves more rapidly than the bigger one, despite the possible degeneracy between latitude and radius (figure 9).

In literature, the photometric study of HD 134319 was presented by [Messina et al. \(1998\)](#) and [Messina & Guinan \(1998\)](#), who analysed HD 134319 LC from 1991 to 1995 and reported a two spot configuration existed over 5 years, despite the large gap between sections. Such a configuration was widely found on other stars with different rotation periods. Rapid rotator AB Dor ($P \sim 0.51479$ day, K0V, $70 \sim 100$ Myrs) was reported to maintain two long-lasting longitudes over tens of years from long-term photometry (e.g. [Berdyugina & Järvinen 2005](#); [Ioannidis & Schmitt 2020](#)) and evolving SDR from Dopple imaging (e.g. [Donati & Collier Cameron 1997](#); [Petit et al. 2002](#); [Collier Cameron & Donati 2002](#); [Jeffers et al. 2007](#)) as well as ultra-active phenomena like superflares ([Schmitt et al. 2019](#)). The rapidly rotating M4 type star GJ 1243 ($P \sim 0.59$ day, mass $\sim 0.24 M_\odot$) was found to be dominated by one stable and another evolving active longitudes during Kepler and TESS epoch ([Davenport et al. 2020](#)). Detailed studies on FK Com ($P \sim 2.4$ day, G4III) revealed two active regions with apparently different sizes and their "flip-flop", phase-jumps, spot emerges, drifts and so on (e.g. [Korhonen et al. 2001](#); [Oláh et al. 2006](#); [Hackman et al. 2013](#)). On BY Dra type star LQ Hydrae ($P \sim 1.6$ day, age ~ 60 Myr, K1V), long-term photometry revealed dominance of two active longitudes over 20 years so that "the first evidence of flip-flop on single dwarf" and multiple activity cycles, in both non-axisymmetric and axisymmetric (as in the Sun) modes, in time-length of years were reported ([Berdyugina et al. 2002](#); [Lehtinen et al. 2012](#)). Another analogy, Kepler-17 (with slower rotation, $P \sim 12.01$ day, G2V) also showed two active longitudes, one of them survived over Kepler's observation period, and an evidence of cycle ([Lanza et al. 2019](#)). Thus one can reasonably expect that such a two spot configuration exists widely on stars, and we can suggest an internal non-axisymmetric geometry for HD 134319, possessed by almost constant mean field configuration which was believed to indicate a small differential rotation ([Messina & Guinan 1998](#)).

4.2.2 Rotational modulation periods of starspots

As shown in figures 8 and 11, the spot configuration on HD 134319 revealed long-lasting features as well as significant evolution in their locations and sizes. For easier discussion, we divided the observation time into two durations, i.e. "T1", from 1683 to 1764 (sectors 14–16) and the other "T2", from 1869 to 1955 (sectors 21–23). The primary region "P" tended to be a long-lasting feature undergoing slow evolution from "T1" to "T2", while the secondary region "S" migrated not

too much in "T1", like "P", but exhibit a much rapid evolution in "T2".

The rotational modulation period of individual spot can be measured from the phased LC ([Davenport et al. 2015](#)) by fitting its longitude with a linear function

$$P_i = P_0 / (1 - m_i P_0) \quad (4)$$

where P_0 is the phase folding period, the subscript i represents the index of spot and m_i is the slope. Note by this definition a negative slope yields a smaller value than P_0 .

The fittings are overlaid in figure 11 with three lines. Fitting of "P" gave an average rotational modulation period of $P_P = 4.4236654 \pm 0.0003350$ day, starting at phase about $\lambda_P = 0.71$ at epoch 1683 (red line). Fitting of "S" in "T1" gave $P_{S1} = 4.4226344 \pm 0.0016632$ day and $\lambda_{S1} = 0.34$ at epoch 1683 (blue dashed line). And fitting of "S" in "T2" gave $P_{S2} = 4.3580376 \pm 0.0064554$ day and $\lambda_{S2} = 0.19$ at epoch 1689 (dark dash-dot line). P_P and P_{S1} were estimated with high confidence due to their stabilities, however P_{S2} was determined with larger uncertainty due to its rapid evolution. Note that these values are smaller than the phase folding period, i.e. $P_0 = 4.436391$ day, derived by GLS determination of the whole LC.

4.2.3 Starspot evolution

The deviation of spot longitude from its rotational modulation period represents the spot longitudinal migration from average location, as shown in figure 12. In "T1", the two spots exhibited highly synchronized oscillatory variations with amplitude of about 15° and period of about 40 days. This phenomenon can also be seen in figure 2 where the two dips in LC varied periodically with time. In "T2", "P" remained the same level of evolution like before, however "S" underwent a much sudden evolution than "T1", i.e. it had an obviously small average rotational period than "P" and exhibited a much larger longitudinal oscillation with amplitude of about 40° and period of 30–40 days, which broke the previous synchronization and seemed to be a new distribution of the spot feature. This indicates that "P" survived over time spanning from "T1" to "T2", while "S" survived over "T1" but might be a new one in "T2".

On the other hand, although correlated with recovered latitudes as shown in figure 9, the spot sizes were found to evolve with time in terms of relative variations. Firstly, compared with a supposed spot located at average latitude $\beta = 70^\circ$, "P" has a maximal radius of about 28° in "T1" and decreases to about 20° in "T2", while "S" has an average radius of about 23° in "T1" and a smaller radius of only 13° in "T2". So the spot configuration was likely to be dominated by one larger plus a smaller active region, and both of them decreased to smaller scales from "T1" to "T2", in the sense of projected area. Secondly, as shown in figure 8, "S" radius in "T1" increased rapidly around epoch 1692 from 26° to 31° and then decreased gradually to small value of about 12° at the end of "T1", which was in similar size as in "T2", while "P" underwent an opposite variation which had a rapid decrease at epoch 1692 from 29° to 22° followed by a gradually recovery to large size. For the case of "T2", in contrary, the two spots showed synchronized variation of radii over time.

Considering the spot radius-latitude correlation, the variations in "T2" might result from the parameter degeneracy

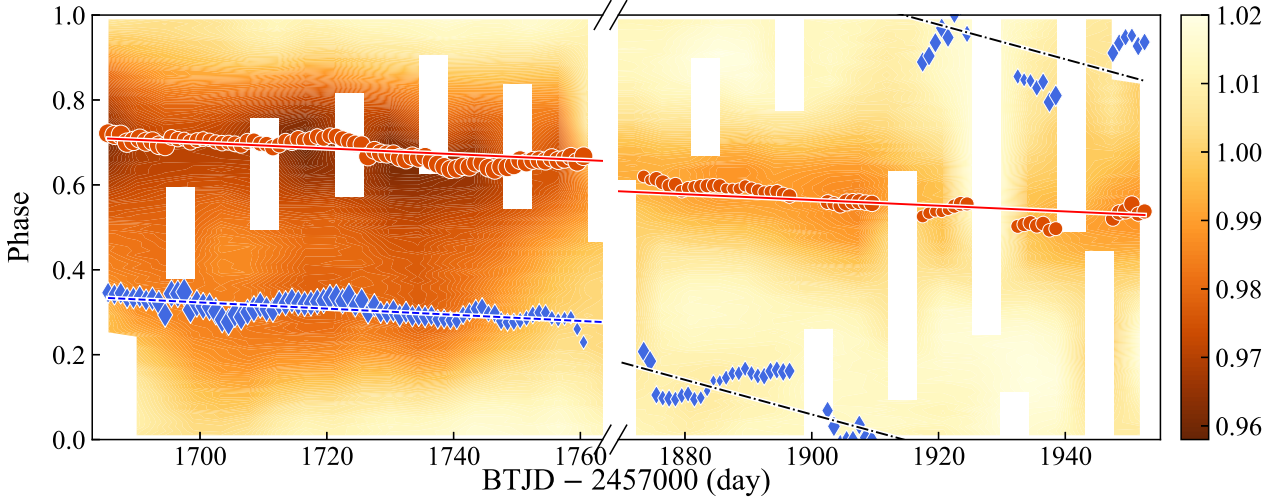


Figure 11. Continuous phased LC map of the entire TESS long cadence data set with period $P = 4.436391$ day, with the spot longitudes from our two spot model as well as their linear fittings overlaid. The pixel shade, from dark to light, indicates the flux in each (time/phase) chunk, and is interpolated and plotted as contour map. Vertical white gaps correspond to times with no TESS data, and the long-time gap of observation are marked as breaks in horizontal axes. The longitude corresponding to the primary active region, "P", and its linear fitting are overlaid with orange circles and red line, while the longitude corresponding to the secondary active region, "S", and its linear fittings to the first and last half data separately, are overlaid with blue diamonds, blue dashed and dark dash-dot lines, respectively. The symbols are scaled proportional to the spot radii.

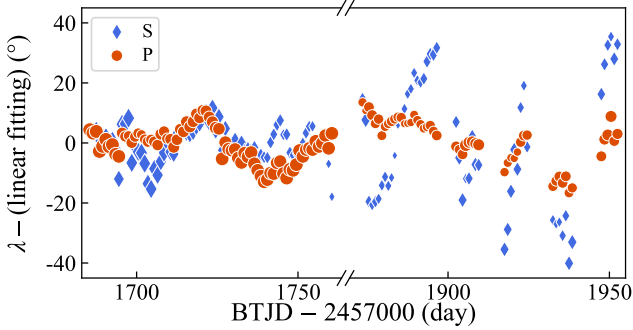


Figure 12. Subtraction of spot longitude (λ) by its linear fitting, $\lambda - (\text{linear fitting})$, i.e. spot longitudinal migration from its average location, versus time. The symbols are scaled proportional to the spot radii, as in figure 11.

due to weak constraints of photometry, however one can still recognize two evidences of spot evolution in "T1" with reliability. One is the simultaneous but opposite variations between "P" and "S" around 1692, which indicates either a switch of the activity level from one spot to another or the latitudinal migration to opposite directions. This phenomenon was also reported and analysed in detail on HQ Hydrae by Lehtinen et al. (2012) who discriminated the "flip-flop" from more commonly "switch" phenomenon. The other is the decrease of "S" since 1720.

Figure 13 presents the long-term evolution of the LC mean brightness M and peak-to-peak amplitude A , which were usually employed in estimating the stellar activity variations due to spots (Berdyugina et al. 2002; Lehtinen et al. 2012; Ioannidis & Schmitt 2020). The variation in M could be explained by activity difference, or spot size variations, between "T1"

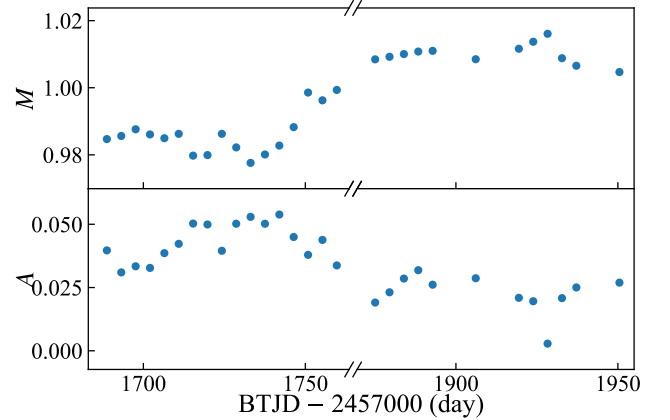


Figure 13. The long term variation of the mean brightness M (top) and peak-to-peak amplitude A (bottom) of HD 134319 measured from figure 2.

and "T2". While the decrease in A attributes mainly to the decay of spot "P" to small size from "T1" to "T2", supporting the above analysis.

Considering the coherence of the spot longitudinal migration and radial evolution, the primary active region "P" is likely to be the same one which migrated and oscillated from phase 0.71 and lived longer than the observation season (280 days), while the secondary active region "S" exhibited different types of evolution and thus is likely to represent different spot features at least between "T1" and "T2". This inference is in accordance with the scenario that spot lifetime is proportional to its size and large spot can survive for many years (see reviews of Berdyugina (2005) and Strassmeier (2009)).

4.2.4 Differential rotation

Despite the weak constraint on spot latitude, the multiple rotational modulation periods in abundant photometric time series were widely taken as indicator of SDR on many stars other than the Sun. By assuming the latitudinal occupation of spots towards both equator and pole as much as possible, the seasonal period variation from extreme long-term photometry was applied to estimate the lower-limit of SDR (e.g. Henry et al. 1995; Messina & Guinan 2003; Balona & Abedigamba 2016). At the mercy of precise photometric data, there exist studies attempting to inverse spot rotational modulation period and latitude simultaneously and thus directly estimating the SDR (e.g. Croll et al. 2006; Fröhlich et al. 2012; Lanza et al. 2016). However, studies aiming at examining the reliability of SDR detection based on photometry alone revealed the probability of misleading results especially in evolving stages (Aigrain et al. 2015; Basri & Shah 2020).

The difference of spot rotational modulation periods between "P" and "S" in "T1" is quite small, i.e. $\Delta P = 0.0010310 \pm 0.0016966$ day, corresponding to a lower-limit of SDR as $\alpha = 0.000233$. Meanwhile, the difference between "P" and "S" in "T2" yields $\Delta P = 0.0656278 \pm 0.0064641$ day, corresponding to a lower-limit of SDR as $\alpha = 0.0148$, which is apparently smaller than prediction from statistics (Reinhold et al. 2013; Balona & Abedigamba 2016) and dynamo studies (Küker & Rüdiger 2008; Kitchatinov & Olemskoy 2012). Such a small difference is probably due to the nearby latitudinal distribution of spots during the observation season (or, spot pair is located on opposite hemispheres, which is indistinguishable in the case of inclination $i = 90^\circ$). As in figure 8, the best-fitted spot latitudes were close to each other, i.e. between $\beta = 50^\circ$ and 85° and varied temporally not too much, supporting above situation.

Due to the weak constraint of photometric observation on latitudinal information and the possible migration of starspots, the estimation of SDR is pretty difficult. The lower limit of SDR shear is reliable only when the magnetic configuration can be described by such a two-spot model and all starspots are centered in certain longitudes, however both of which cannot be confirmed from collected data, and thus the above discussion should be treated with caution.

4.3 Chromospheric activity in short and long timescales

The relative equivalent widths (ΔW s) of Ca II H and K, H β and H α lines are listed in table 4 and plotted in figure 14. Observations by OHP/ELODIE within about one year have good phase coverage, the measurements yield typical median uncertainties of 0.036088 for H β and 0.015585 for H α , except two extremely low SNR records 23 and 24. Observations by Keck/HIRES have long time baseline over 14 years but are sparsely sampled, the measurements yield typical median uncertainties of 0.025996, 0.018091, 0.006445, and 0.005927 for Ca II H and K, H β and H α , respectively.

4.3.1 Long-term evolution

As shown in figure 14, during observations in near 20 years, the chromospheric activity indicators show variations exceed

0.1\AA . Evolutions in both short and long timescale are discriminable by comparing their relative variations of equivalent widths in different timescales. The short-term evolution within one or a few rotations can be attributed to the rotational modulation as revealed by OHP/ELODIE observation with good phase coverage, which will be discussed in more detail in section 4.3.3. While the notable variation in Keck/HIRES observing season shows the maximal scale, indicating evolution in long timescale. Linear fitting of H β (overlaid by green dashed line) reveals a trend of its average ΔW from -0.012 to 0.011\AA with time, implying a decrease of activity level in long timescale.

4.3.2 Correlations between indicators

Correlations between chromospheric activity indicators were widely studied on active stars (e.g. Strassmeier et al. 1990; Montes et al. 1995; Cincunegui et al. 2007; Martínez-Arnáiz et al. 2011; Scandariato et al. 2017). The excess emissions of Ca II H and K (3968 and 3933 \AA) resonance were found to be tightly correlated with each other and thus were practically measured together, for example, the widely used S-index (Duncan et al. 1991), in estimating the stellar activity. Two other well studied chromospheric proxies, H α (6363 \AA) and H β (4861 \AA) lines, which can be feasibly measured with high SNR on even pretty cool stars where the Ca II resonance becomes progressively faint, resulted from the two most probable transitions of electrons between energy levels of Hydrogen which is the most abundant element inside the Sun and other stars, were also found to be correlated with each other. However, correlation between H α and Ca II resonance was more complicated, because H α reveals not only a non-monotonically variation with increasing heating rate (Linsky 2017) but also the dependence on stellar physical parameters such as pressure and temperature (Cincunegui et al. 2007).

Figure 15 shows the correlation between ΔW s of Ca II K and H, H β and H α lines. Linear fitting to each relation was done for estimating the relative difference between indicators and overlaid in this figure by dashed line. Note by the linear fitting a positive slope yields a positive correlation. We can find that the relative variation of any indicator is strongly correlated with the others, despite the quantitatively different uncertainty levels.

Due to the lack of comparing star as template, it is difficult to estimate the absolute value of H β and H α emissions, while we can estimate equivalent widths of Ca II H and K lines due to their narrow emission profiles. Measurements gave $W_H = -0.342627\text{\AA}$ and $W_K = -0.581948\text{\AA}$ for Ca II H and K lines, respectively, by directly integrating their overall spectra over 1.1\AA width portions centred on the emission cores, and yielded a ratio of $W_K/W_H = 1.698487$ which is close to the slope of linear fitting (top panel in figure 15). This infers that the relative variations of Ca II H and K lines are proportional to their respective absolute emission strengths.

The larger variation of H α than H β in bottom panel of figure 15 could be attributed to its lower energy required in electron transitions in principle, while the more commonly mentioned correlation between Ca II and H α lines was found to depend on stellar parameters such as the stellar effective temperature, metallicity and pressure etc. (e.g. Cincunegui et al. 2007; Walkowicz & Hawley 2009; Scandariato et al. 2017). By analogy to the study on the Sun by Gebbie & Steinitz

Table 4. The relative equivalent widths measured from the residual spectra, which represent the difference between individual spectrum and the overall spectrum for each chromospheric activity indicator (see section 3.2). The last column is the instrument, "E" represents OHP/ELODIE and "H" represents Keck/HIRES.

No.	Date yyyymmdd	Epoch MJD-50000	ΔW_K (\AA)	ΔW_H (\AA)	$\Delta W_{H\beta}$ (\AA)	$\Delta W_{H\alpha}$ (\AA)	Inst.
1	19951106	27.758241	-0.031373±0.040562	-0.018857±0.015511	E
2	19960503	206.975949	-0.029332±0.027837	-0.033498±0.013834	E
3	19960503	206.989294	-0.030835±0.026398	-0.030377±0.013863	E
4	19960504	208.035718	-0.027873±0.021146	-0.029040±0.010667	E
5	19960505	209.994572	-0.015346±0.020592	-0.032421±0.010319	E
6	19960506	210.940266	-0.017242±0.026576	-0.013584±0.010882	E
7	19960508	212.998855	-0.040752±0.032760	-0.021943±0.016166	E
8	19960628	262.953877	-0.018798±0.036594	-0.001461±0.016825	E
9	19960628	262.962755	-0.025168±0.039243	-0.004372±0.017009	E
10	19960629	263.881146	-0.035705±0.035581	-0.022479±0.016555	E
11	19960629	263.890013	-0.039269±0.037212	-0.027851±0.015313	E
12	19960630	264.888473	-0.030101±0.033388	-0.038060±0.015731	E
13	19960630	264.897384	-0.018138±0.038456	-0.034214±0.016794	E
14	19960701	265.879850	-0.011007±0.031238	-0.006143±0.014964	E
15	19960701	265.892223	-0.020166±0.038616	-0.014393±0.017049	E
16	19960702	266.930995	-0.051228±0.070634	-0.042379±0.024720	E
17	19960702	266.939896	-0.021975±0.074569	-0.004292±0.023377	E
18	19960703	267.924133	-0.006526±0.037805	0.009826±0.015257	E
19	19960703	267.932987	-0.023558±0.042209	0.010922±0.015659	E
20	19960828	323.834537	-0.024840±0.051999	-0.022079±0.017712	E
21	19960829	324.823485	-0.026197±0.029949	-0.025716±0.012245	E
22	19960901	327.855637	-0.031695±0.033460	-0.015077±0.013060	E
23	19961229	447.207779	-0.197406±0.339053	0.181427±0.068684	E
24	19970125	474.192547	-0.128411±0.360773	0.169545±0.141722	E
25	19970128	477.205753	-0.019608±0.031867	0.001652±0.019156	E
26	19970129	478.191632	-0.022774±0.019649	-0.019219±0.009338	E
27	19990424	1292.561160	-0.084215±0.069323	-0.034360±0.031120	-0.035413±0.007033	...	H
28	19990425	1293.526583	-0.001237±0.068204	-0.013785±0.054094	-0.026791±0.011333	...	H
29	19990519	1317.430287	0.008699±0.045056	0.000250±0.036867	0.001960±0.009238	...	H
30	19990808	1398.261886	0.023564±0.053873	0.000142±0.041517	0.007955±0.010172	...	H
31	20030114	2653.679294	0.054104±0.027859	0.031481±0.017816	0.022237±0.005083	...	H
32	20030314	2712.478795	-0.025440±0.028476	-0.012997±0.018487	-0.014811±0.005179	...	H
33	20030616	2806.324191	0.004558±0.017696	0.005198±0.010904	0.000763±0.003301	...	H
34	20030616	2806.375226	0.020166±0.024592	0.007891±0.017010	0.010546±0.006181	...	H
35	20030713	2833.330383	0.004602±0.016301	0.001800±0.010753	0.005014±0.004157	...	H
36	20030728	2848.266842	0.043567±0.016419	0.022013±0.013506	0.019795±0.004684	...	H
37	20040625	3181.446408	-0.091720±0.017171	-0.058185±0.011094	-0.025069±0.004413	...	H
38	20040710	3196.314068	0.002408±0.053364	-0.010890±0.043795	0.006985±0.009848	...	H
39	20050225	3426.617754	-0.023167±0.022615	-0.017766±0.015543	-0.001114±0.005827	-0.003765±0.005488	H
40	20060416	3841.393636	-0.038543±0.022988	-0.027235±0.017408	-0.021964±0.006786	-0.028862±0.005404	H
41	20080127	4492.683551	0.006933±0.019474	0.005565±0.013863	0.009798±0.005215	0.030829±0.004608	H
42	20090604	4986.408533	0.033238±0.038755	0.020317±0.027897	0.012719±0.010399	0.055268±0.008783	H
43	20100204	5231.671857	-0.034793±0.026827	-0.022060±0.017126	-0.009158±0.008149	-0.020032±0.005889	H
44	20110615	5727.448702	0.050378±0.044145	0.023823±0.030052	0.028416±0.012267	0.094395±0.010165	H
45	20110615	5727.458635	0.058932±0.042421	0.033285±0.027970	0.018301±0.010821	0.063508±0.008704	H
46	20120305	5991.668097	-0.012412±0.025164	-0.006934±0.018366	0.002887±0.006191	0.002646±0.006686	H
47	20120601	6079.331947	0.011411±0.019098	0.003193±0.013857	0.008064±0.005063	0.048057±0.005655	H
48	20130709	6482.252854	-0.043213±0.024948	-0.020351±0.022389	-0.003531±0.006699	-0.010131±0.005964	H

(1974), who proposed that the formation of Ca II is direct collision dominated due to turbulent velocities while the formation of H α is photoionization dominated due to radiation which decreases in late-type stars, one could reasonably expect different correlations between Ca II and H α on different type of stars. Thus the ratio between Ca II and H α (simply as $(\Delta W_K + \Delta W_H)/\Delta W_{H\alpha} \sim 2.238$) is larger than one, might indicate that the chromospheric excitation on HD 134319 is dominated by collision due to turbulent velocities.

4.3.3 Rotational modulation of indicators

In short timescale, variations of chromospheric proxies under rotational modulation were widely reported on stars (e.g. Wright et al. 2004; Isaacson & Fischer 2010; Flores Soriano & Strassmeier 2017). Such variations can also be found on HD 134319. Figure 16 shows the phase folded ΔW s of Ca II H and K, H β and H α within chosen time durations no longer than half a year. Among the five durations, (a) and (b) have good phase coverage in about one rotation cycle, while (c) –

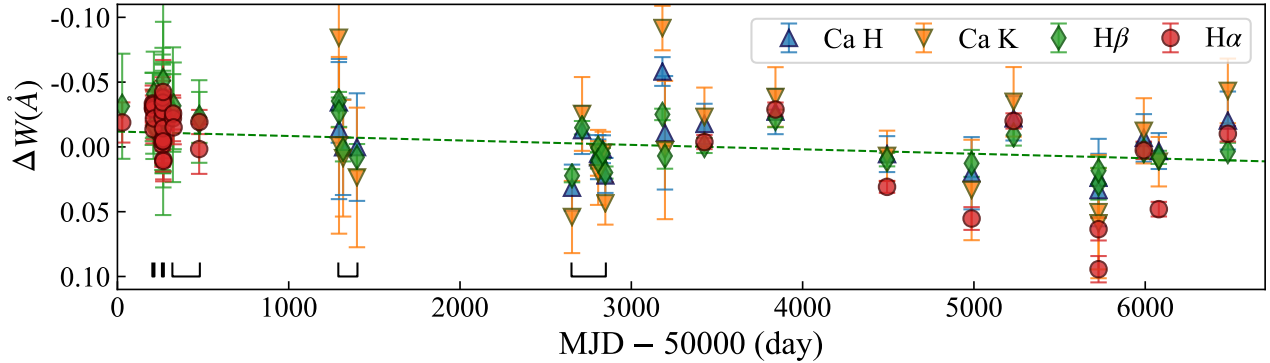


Figure 14. The relative equivalent widths versus time as table 4. The linear fitting on $H\beta$ is overlaid with dashed line, and the time durations used for analysing rotational modulation (figure 16) are marked with dark lines. Hereafter, the axis corresponding to equivalent widths is inverted for easier view.

(f) are phase-folded for data collected in months. With the good phase coverage of OHP/ELODIE observations, two peaks around phases 0.2 and 0.7 are recognizable from panels (a) – (b) during time from May to July of 1996, corresponding to two active regions characterized by enhancement of chromospheric emissions. Later, for the precise data observed by Keck/HIRES in year 1999 and 2003, at least one active region around phase 0.4 can be recognized, despite the poor phase coverage.

The long-term behaviour of the chromospheric emissions under rotational modulation implies that HD 134319 was dominated by two active regions during years from 1996 to 1997, and the peak around phase 0.2 – 0.4 might be due to a long-lived active region lasting over years from 1996 to 2003.

4.3.4 Connection between chromospheric activity and photospheric spots

The possible connection between chromospheric activity and photometric variation would indicate a configuration of the magnetic field spreading over photosphere and chromosphere. A clear anti-correlation between them on LQ Hydrae was reported and interpreted as the spatial connection between photospheric dark spots and chromospheric plages (Cao & Gu 2014; Flores Soriano & Strassmeier 2017), the similar phenomenon was also reported on FK Comae (Vida et al. 2015).

It is difficult to analyse this relation exactly on HD 134319 due to the lack of overlap between photometric and spectroscopic observations analyzed in this paper. In figure 16 (a) and (b), we over-plot the phased LC taken from figure 3 of Messina et al. (1998) observed around 1995.38, which is the closest to the spectroscopic data in time, separated by more than one year. A positive correlation between ΔW and inverted photometric LC can be found but at low significance. Thus no reliable conclusions can be concluded with collected data.

5 SUMMARY

In this paper, we present the analysis of the starspot configuration, evolution and chromospheric activity on HD 134319,

by employing the high precision photometry by space-based TESS telescope in sectors 14–16 (epoch 1683–1764, called "T1") and 21–23 (epoch 1869–1955, "T2") and the spectroscopic data observed by OHP/ELODIE and Keck/HIRES from year 1995 to 2013.

We firstly measured the rotation period of the star from TESS LC as $P = 4.436391 \pm 0.00137$ days which is used in subsequent analysis, using GLS method (Zechmeister & Kürster 2009). Then, the starspot configurations at series of epochs were derived by splitting the whole TESS LC into 129 chunks in 5 days length and then fitting them separately with a two-spot model. Besides, based on analysis of the high-resolution spectroscopic data, we derived the relative equivalent widths (ΔW s) of the Ca II H and K, $H\beta$ and $H\alpha$ lines to investigate its chromospheric activity.

We focus on magnetic characteristics on HD 134319 using a simple two-spot model. One should keep in mind that the actual number of starspots (or active regions) could not be decided with collected data and might much larger than the number of dips in LC. However our model revealed reasonable good fits, and if the star really has only two spots or can be described by such a model, it would be the result. Our main results are summarized as follows:

(I) As revealed by analysis of TESS LC data, a two-spot configuration, i.e., a long-lasting primary spot "P" plus a secondary spot "S", was capable of explaining the LC variation on HD 134319 during observation. Furthermore, the primary spot was likely to survive at least longer than TESS observation duration, i.e. 300 days, and might survive over years.

(II) Linear fittings on spot longitudes give the average rotational modulation period of spots as: $P_P = 4.4236654 \pm 0.0003350$ day emerging at phase $\lambda_P = 0.71$ at epoch 1683, $P_{S1} = 4.4226344 \pm 0.0016632$ day emerging at phase $\lambda_{S1} = 0.34$ at epoch 1683 and $P_{S2} = 4.3580376 \pm 0.0064554$ day emerging at phase $\lambda_{S2} = 0.19$ at epoch 1689. This corresponds to a low-limit of SDR, if starspots underwent no migration at long-time scale, as $\alpha = 0.0148$ which is weaker than prediction, which might due to a nearby distribution of spot latitudes.

(III) Reliable evolutions of spot radii can be derived despite the radius-latitude degeneracy (figures 8 and 9). A sudden increase of "S" from radius $\gamma = 26^\circ$ to 31° and simultaneous sudden decrease of "P" from $\gamma = 29^\circ$ to 22° around epoch

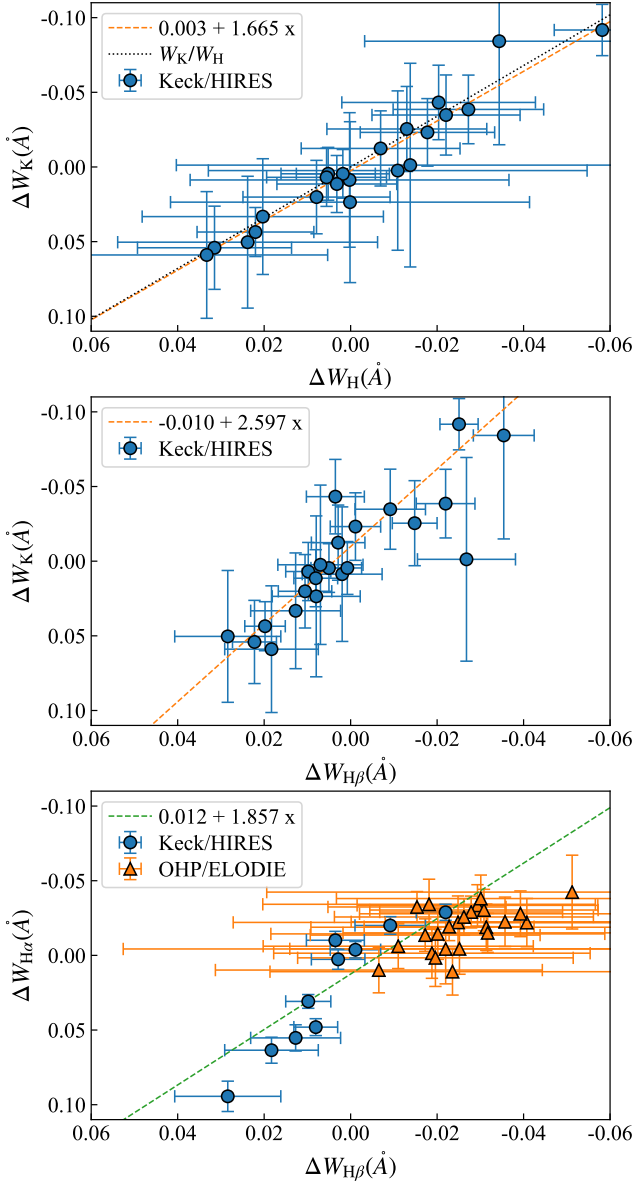


Figure 15. Relative equivalent widths of Ca II K versus H (top), Ca II K versus H β (middle) and H α versus H β (bottom), the uncertainties are plotted by horizontal and vertical errorbars, respectively. Weighted linear fittings are overlaid with dashed lines, the ratio of $W_K/W_H \sim 1.698487$ is overlaid with dark dots.

1692 indicate an exchange of activity strength between spots. Since epoch 1692, "S" radius underwent a gradual decrease to about 12° at the end of "T1", similar to its radius in "T2". Besides, decrease of spot radii from epoch 1683 – 1764 to 1869 – 1955 was notable (figure 9). Comparing with a reference spot at latitude $\beta = 70^\circ$, "P" had radius $\gamma \sim 28^\circ$ and "S" had radius $\gamma \sim 23$ in epoch 1683 – 1764, while "P" had radius $\gamma \sim 20^\circ$ and "S" had radius $\gamma \sim 13^\circ$ in epoch 1869 – 1955. This indicates the decrease of magnetic activity from epoch 1683 – 1764 to 1869 – 1955.

(IV) The spots also exhibited longitudinal migrations. "P" evolved slowly and migrated in oscillation around its average longitude with amplitude of about 15° and period of about

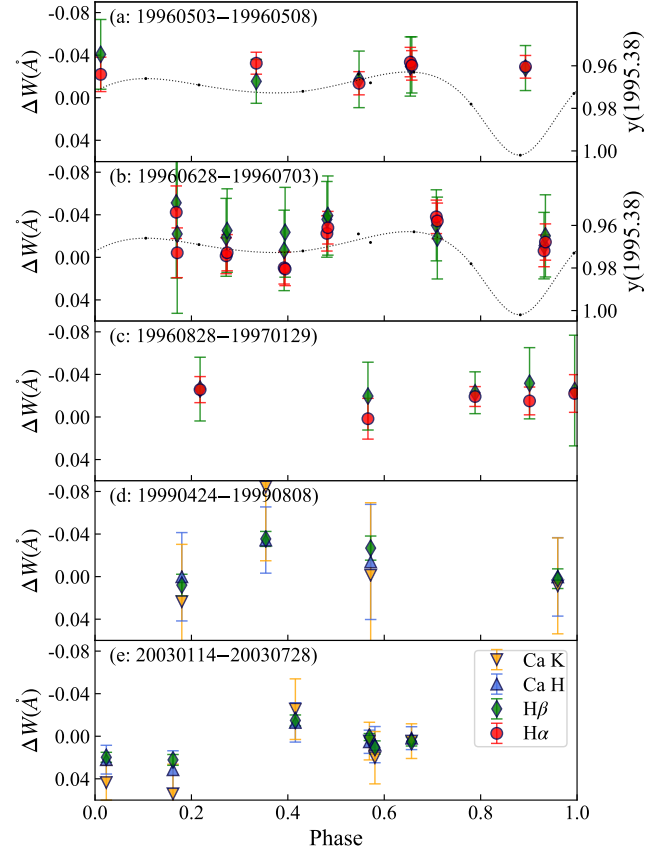


Figure 16. Phase-folded relative equivalent widths (ΔW s) of Ca II K and H, H β and H α lines in five chosen time durations shorter than half a year (marked in figure 14). Peaks in the phased curves represent the phase of enhanced chromospheric emissions under rotational modulation. Moreover, the y-band LC taken from figure 3 of Messina et al. (1998) is re-folded by newly measured rotation period and plotted in (a) and (b) with dark dots, overlaid by smoothed dotted lines, and is inverted so that the possible spatial connection between chromospheric emissions and photospheric spots is manifested as the positive correlation between inverted ΔW and LC.

40 days, "S" in "T1" showed migration tightly synchronized with "P", while "S" in "T2" showed much larger oscillation with amplitude of about 40° and period of 30 – 40 days (figures 11 and 12).

(V) Relative variations of chromospheric activity indicators from 1995 to 2013 revealed both short-term rotational modulation (figure 16) and long-term decrease of activity (figure 14), implying the existence and evolution of magnetic activity, and thus the distortion of LC is likely due to starspots on HD 134319.

ACKNOWLEDGMENTS

This research has made use of the SIMBAD database, operated at CDS, Strasbourg, France (<http://cdsweb.u-strasbg.fr/>), the data from the European Space Agency (ESA) mission *Gaia* (<https://www.cosmos.esa.int/gaia>), processed by the *Gaia* Data Processing and Analysis Con-

sortium (DPAC, <https://www.cosmos.esa.int/web/gaia/dpac/consortium>), the Keck Observatory Archive (KOA), which is operated by the W. M. Keck Observatory and the NASA Exoplanet Science Institute (NExScI), under contract with the National Aeronautics and Space Administration and the ELODIE archive at Observatoire de Haute-Provence (OHP, <http://atlas.obs-hp.fr/elodie/>). Funding for the DPAC has been provided by national institutions, in particular the institutions participating in the *Gaia* Multilateral Agreement. TESS photometric data presented in this paper were obtained from the Mikulsky Archive for Space Telescopes (MAST). STScI is operated by the Association of Universities for Research in Astronomy, Inc., under NASA contract NAS5-26555. This paper includes data collected by the TESS mission. Funding for the TESS mission is provided by the NASA's Science Mission Directorate. We made use of LIGHTKURVE, a Python package for Kepler and TESS data analysis (Lightkurve Collaboration et al. 2018) launched in Jupyter Notebook environment (<https://github.com/jupyter/notebook/>), built on top of libraries including NUMPY (Harris et al. 2020), SCIPY (Virtanen et al. 2020) and MATPLOTLIB (Hunter 2007) and relative to ASTROPY (Astropy Collaboration et al. 2018), ASTROQUERY (Ginsburg et al. 2019), CELERITE (Foreman-Mackey et al. 2017) and TESSCUT (Brasseur et al. 2019). NUMPY, MATPLOTLIB, SCIPY and BROKENAXES (<https://github.com/jerrylikeric/brokenaxes>) were used in preparing figures of this paper. We also thank Dr. Longcheng Gui[✉] for his great help in computing resources. This work is supported by National Natural Science Foundation of China through grants Nos. 10373023, 10773027, 11333006, U1531121, and 11903074. We acknowledge the science research grant from the China Manned Space Project with NO. CMS-CSST-2021-B07. The joint research project between Yunnan Observatories and Hamburg Observatory is funded by Sino-German Center for Research Promotion (GZ1419).

DATA AVAILABILITY

The data underlying this article are available in the article. Part of the data underlying this paper are in the public domain and available in: the Gaia Archive (<https://gea.esac.esa.int/archive/>), the Keck Observatory Archive (KOA; <https://koa.ipac.caltech.edu/>), the ELODIE Archive (<http://atlas.obs-hp.fr/elodie/>) and Mikulski Archive for Space Telescopes (MAST; <https://archive.stsci.edu>).

REFERENCES

- Aigrain S., et al., 2015, *MNRAS*, **450**, 3211
 Astropy Collaboration et al., 2018, *aj*, **156**, 123
 Auvergne M., et al., 2009, *A&A*, **506**, 411
 Balona L. A., Abedigamba O. P., 2016, *MNRAS*, **461**, 497
 Balona L. A., et al., 2019, *MNRAS*, **485**, 3457
 Baranne A., et al., 1996, *A&AS*, **119**, 373
 Barden S. C., 1985, *ApJ*, **295**, 162
 Basri G., Shah R., 2020, *ApJ*, **901**, 14
 Batalha N. M., et al., 2010, *ApJ*, **713**, L109
 Berdyugina S. V., 2005, *Living Reviews in Solar Physics*, **2**, 8
 Berdyugina S. V., Järvinen S. P., 2005, *Astronomische Nachrichten*, **326**, 283
 Berdyugina S. V., Pelt J., Tuominen I., 2002, *A&A*, **394**, 505
 Boro Saikia S., et al., 2018, *A&A*, **616**, A108
 Brasseur C. E., Phillip C., Fleming S. W., Mullally S. E., White R. L., 2019, Astrocut: Tools for creating cutouts of TESS images (ascl:1905.007)
 Budding E., 1977, *Ap&SS*, **48**, 207
 Burgasser A. J., Kirkpatrick J. D., Lowrance P. J., 2005, *AJ*, **129**, 2849
 Butler R. P., et al., 2017, *AJ*, **153**, 208
 Cao D.-t., Gu S.-h., 2014, *AJ*, **147**, 38
 Cao D., et al., 2019, *MNRAS*, **482**, 988
 Cincunegui C., Díaz R. F., Mauas P. J. D., 2007, *A&A*, **469**, 309
 Claret A., 2018, *A&A*, **618**, A20
 Collier Cameron A., Donati J. F., 2002, *MNRAS*, **329**, L23
 Croll B., et al., 2006, *ApJ*, **648**, 607
 Davenport J. R. A., Hebb L., Hawley S. L., 2015, *ApJ*, **806**, 212
 Davenport J. R. A., Mendoza G. T., Hawley S. L., 2020, *AJ*, **160**, 36
 Decin G., Dominik C., Waters L. B. F. M., Waelkens C., 2003, *ApJ*, **598**, 636
 Donati J. F., Collier Cameron A., 1997, *MNRAS*, **291**, 1
 Dorren J. D., 1987, *ApJ*, **320**, 756
 Duncan D. K., et al., 1991, *ApJS*, **76**, 383
 Eberhard G., Schwarzschild K., 1913, *ApJ*, **38**, 292
 Flores Soriano M., Strassmeier K. G., 2017, *A&A*, **597**, A101
 Foreman-Mackey D., Agol E., Angus R., Ambikasaran S., 2017, ArXiv
 Fröhlich H. E., Frasca A., Catanzaro G., Bonanno A., Corsaro E., Molenda-Żakowicz J., Klutsch A., Montes D., 2012, *A&A*, **543**, A146
 Gaia Collaboration 2018, VizieR Online Data Catalog, p. I/345
 Gaia Collaboration et al., 2016, *A&A*, **595**, A1
 Gaia Collaboration et al., 2018, *A&A*, **616**, A1
 Gebbie K. B., Steintz R., 1974, in Athay R. G., ed., Vol. 56, Chromospheric Fine Structure. p. 55
 Ginsburg A., et al., 2019, *AJ*, **157**, 98
 Gu S.-h., Tan H.-s., Shan H.-g., Zhang F.-h., 2002, *A&A*, **388**, 889
 Hackman T., et al., 2013, *A&A*, **553**, A40
 Harris C. R., et al., 2020, *Nature*, **585**, 357
 Hempelmann A., Mittag M., Gonzalez-Perez J. N., Schmitt J. H. M. M., Schröder K. P., Rauw G., 2016, *A&A*, **586**, A14
 Henry G. W., Eaton J. A., Hamer J., Hall D. S., 1995, *ApJS*, **97**, 513
 Hunter J. D., 2007, *Computing in Science & Engineering*, **9**, 90
 Işık E., Schmitt D., Schüssler M., 2011, *A&A*, **528**, A135
 Ioannidis P., Schmitt J. H. M. M., 2020, *A&A*, **644**, A26
 Isaacson H., Fischer D., 2010, *ApJ*, **725**, 875
 Jeffers S. V., Keller C. U., 2009, in Stempels E., ed., American Institute of Physics Conference Series Vol. 1094, 15th Cambridge Workshop on Cool Stars, Stellar Systems, and the Sun. pp 664–667, doi:10.1063/1.3099201
 Jeffers S. V., Donati J.-F., Collier Cameron A., 2007, *MNRAS*, **375**, 567
 Jenkins J. M., et al., 2016, in Chiozzi G., Guzman J. C., eds, Society of Photo-Optical Instrumentation Engineers (SPIE) Conference Series Vol. 9913, Software and Cyberinfrastructure for Astronomy IV. p. 99133E, doi:10.1117/12.2233418
 Kervella P., Arenou F., Mignard F., Thévenin F., 2019, *A&A*, **623**, A72
 Kitchatinov L. L., Olemskoy S. V., 2012, *MNRAS*, **423**, 3344
 Koch D. G., et al., 2010, *ApJ*, **713**, L79
 Korhonen H., et al., 2001, *A&A*, **374**, 1049
 Küker M., Rüdiger G., 2008, in Journal of Physics Conference Series. p. 012029, doi:10.1088/1742-6596/118/1/012029
 Lanza A. F., Piluso N., Rodonò M., Messina S., Cutispoto G., 2006, *A&A*, **455**, 595
 Lanza A. F., Flaccomio E., Messina S., Micela G., Pagano I., Leto G., 2016, *A&A*, **592**, A140

- Lanza A. F., Netto Y., Bonomo A. S., Parviainen H., Valio A., Aigrain S., 2019, *A&A*, **626**, A38
- Lehtinen J., Jetsu L., Hackman T., Kajatkari P., Henry G. W., 2012, *A&A*, **542**, A38
- Lightkurve Collaboration et al., 2018, Lightkurve: Kepler and TESS time series analysis in Python (ascl:1812.013)
- Linsky J. L., 2017, *ARA&A*, **55**, 159
- López-Santiago J., Montes D., Gálvez-Ortiz M. C., Crespo-Chacón I., Martínez-Arnáiz R. M., Fernández-Figueroa M. J., de Castro E., Cornide M., 2010, *A&A*, **514**, A97
- Lowrance P. J., Nicmos Environments Of Nearby Stars Team STIS 8176 Team 2003, in Martín E., ed., Vol. 211, Brown Dwarfs. p. 295 ([arXiv:astro-ph/0208072](https://arxiv.org/abs/astro-ph/0208072))
- Martin E. C., et al., 2017, *ApJ*, **838**, 73
- Martínez-Arnáiz R., López-Santiago J., Crespo-Chacón I., Montes D., 2011, *MNRAS*, **414**, 2629
- McCarthy C., Zuckerman B., Becklin E. E., 2001, *AJ*, **121**, 3259
- Messina S., Guinan E. F., 1998, Information Bulletin on Variable Stars, **4576**, 1
- Messina S., Guinan E. F., 2003, *A&A*, **409**, 1017
- Messina S., Guinan E. F., Lanza A. F., 1998, *Ap&SS*, **260**, 493
- Messina S., Rodonó M., Guinan E. F., 2001, *A&A*, **366**, 215
- Meyer M. R., et al., 2006, *PASP*, **118**, 1690
- Mittag, M. Schmitt, J. H. M. M. Schröder, K.-P. 2018, *A&A*, **618**, A48
- Mittag M., Schmitt J. H. M. M., Hempelmann A., Schröder K. P., 2019, *A&A*, **621**, A136
- Montes D., Fernández-Figueroa M. J., de Castro E., Cornide M., 1995, *A&A*, **294**, 165
- Montes D., López-Santiago J., Gálvez M. C., Fernández-Figueroa M. J., De Castro E., Cornide M., 2001, *MNRAS*, **328**, 45
- Morris B. M., Curtis J. L., Douglas S. T., Hawley S. L., Agüeros M. A., Bobra M. G., Agol E., 2018, *The Astronomical Journal*, **156**, 203
- Morris B. M., Curtis J. L., Sakari C., Hawley S. L., Agol E., 2019, *The Astronomical Journal*, **158**, 101
- Moultaka J., Ilovaisky S. A., Prugniel P., Soubiran C., 2004, *PASP*, **116**, 693
- Mugrauer M., et al., 2004, *A&A*, **417**, 1031
- Namekata K., et al., 2020, *ApJ*, **891**, 103
- Oláh K., Korhonen H., Kóvári Z., Forgács-Dajka E., Strassmeier K. G., 2006, *A&A*, **452**, 303
- Özavcı I., Şenavcı H. V., Işık E., Hussain G. A. J., O’Neal D., Yılmaz M., Selam S. O., 2018, *MNRAS*, **474**, 5534
- Petit P., Donati J.-F., Collier Cameron A., 2002, *MNRAS*, **334**, 374
- Reinhold T., Reiners A., Basri G., 2013, *A&A*, **560**, A4
- Ricker G. R., et al., 2015, *Journal of Astronomical Telescopes, Instruments, and Systems*, **1**, 014003
- Scandariato G., et al., 2017, *A&A*, **598**, A28
- Scargle J. D., 1982, *ApJ*, **263**, 835
- Schmitt J. H. M. M., Ioannidis P., Robrade J., Czesla S., Schneider P. C., 2019, *A&A*, **628**, A79
- Shkolnik E., Walker G. A. H., Bohlender D. A., Gu P.-G., Kürster M., 2005, *ApJ*, **622**, 1075
- Soderblom D. R., 1985, *AJ*, **90**, 2103
- Soubiran C., et al., 2018, *A&A*, **616**, A7
- Stassun K. G., et al., 2018, *AJ*, **156**, 102
- Still M., Barclay T., 2012, PyKE: Reduction and analysis of Kepler Simple Aperture Photometry data, Astrophysics Source Code Library (ascl:1208.004)
- Strassmeier K. G., 2009, *A&ARv*, **17**, 251
- Strassmeier K. G., Fekel F. C., Bopp B. W., Dempsey R. C., Henry G. W., 1990, *ApJS*, **72**, 191
- Strömgren B., 1966, *ARA&A*, **4**, 433
- Takeda G., Ford E. B., Sills A., Rasio F. A., Fischer D. A., Valenti J. A., 2007, *ApJS*, **168**, 297
- Valenti J. A., Fischer D. A., 2005, *ApJS*, **159**, 141
- Valio A., Estrela R., Netto Y., Bravo J. P., de Medeiros J. R., 2017, *ApJ*, **835**, 294
- Vida K., Korhonen H., Ilyin I. V., Oláh K., Andersen M. I., Hackman T., 2015, *A&A*, **580**, A64
- Vinícius Z., Barentsen G., Gully-Santiago M., Cody A. M., Hedges C., Still M., Barclay T., 2017, KeplerGO/PyKE, doi:10.5281/zenodo.835583, <https://doi.org/10.5281/zenodo.835583>
- Virtanen P., et al., 2020, *Nature Methods*, **17**, 261
- Vogt S. S., et al., 1994, in Crawford D. L., Craine E. R., eds, Proc. SPIE Vol. 2198, Instrumentation in Astronomy VIII. p. 362, doi:10.1117/12.176725
- Walker G., et al., 2003, *PASP*, **115**, 1023
- Walkowicz L. M., Hawley S. L., 2009, *AJ*, **137**, 3297
- Walkowicz L. M., Basri G., Valenti J. A., 2013, *ApJS*, **205**, 17
- White R. J., Gabor J. M., Hillenbrand L. A., 2007, *AJ*, **133**, 2524
- Wilson R. E., Joy A. H., 1950, *ApJ*, **111**, 221
- Wright J. T., Marcy G. W., Butler R. P., Vogt S. S., 2004, *ApJS*, **152**, 261
- Wright N. J., Drake J. J., Mamajek E. E., Henry G. W., 2011, *ApJ*, **743**, 48
- Xu F., Gu S., Ioannidis P., 2021, *MNRAS*, **501**, 1878
- Zechmeister M., Kürster M., 2009, *A&A*, **496**, 577

This paper has been typeset from a $\text{\TeX}/\text{\LaTeX}$ file prepared by the author.